Interpretation of radar signatures observed in SAR images of ice island T-3 by means of backscatter modelling

Wolfgang Dierking[1,4] , Caren Garrity[2] and René O. Ramseier[3]

1. Alfred-Wegener-Institute for Polar and Marine Research
Am Handelshafen 12, W-2850 Bremerhaven, Germany
Phone: +49-471-4831-261 Fax: +49-471-4831-425

2. Microwave Group - Ottawa River
3954 Armitage Ave. PR#1, Dunrobin, Ontario, KOA 1T0, Canada
Phone: +1-613-832-0411 Fax: +1-613-832-0505

3. Atmospheric Environment Service, Ice R&D Group
195 Westbrook Rd., Stittsville, Ontario, Canada K2S 1A4
Phone: +1-613-832-0504 Fax: +1-613-832-0505

ABSTRACT

During 1978 microwave images of the ice island T-3 were obtained from the SEASAT-A synthetic aperture radar (SAR). In 1979 additional images were acquired by the Canada Centre for Remote Sensing Convair CV-580 aircraft which was equipped with an X- and L-band dual polarization SAR. These images are used to investigate the radar backscattering characteristics of T-3 at L-band HH-polarization, L-band HV-polarization, and X-band HH-polarization. Striking signature features are irregular stripes of strong returns in the L-band HH- and HV-images, and ribbed textures of alternating lighter and darker grey tones in the L- and X-band HH-images. Based on in-situ data of surface morphology and ice properties which were gathered on T-3 and other ice islands, different theoretical backscatter modeling approaches are used to investigate contributions of certain structural elements such as fractures, cracks and lake ice lenses on the image signature characteristics. The ribbed textures are caused by a combination of surface and volume scattering processes, and the stripes of strong returns at L-band are explained by assuming the presence of fracture assemblages in the basement ice of T-3.

1. INTRODUCTION

Ice Island T-3, also known as Fletcher's Ice Island, was discovered in 1950 about 650 km north-west of Point Barrow, Alaska. T-3 was a tabular mass of freshwater ice with dimensions of 8.1 by 16.1 km measured at the time of discovery, and 7 by 14 km measured in 1978. The island's thickness decreased steadily from 60 m in 1952 to 30 m in 1973 due to melting processes at the surface and the bottom. T-3 probably calved from the ice shelves on the North Coast of Ellesmere Island, Canada, after 1935. The positions of T-3 were recorded almost continuously from 1952 to 1979. During that time the drift pattern of the island corresponded to the Beaufort Gyre. Later, the island followed the Transpolar Drift and left the Arctic Ocean. An ice island, believed to be a remnant of T-3, was sighted at the southern tip of Greenland during the summer of 1984 (Jeffries, 1992).

In 1978, T-3 was imaged on a number of occasions with the SEASAT-A synthetic aperture radar (SAR). In 1979, additional SAR imagery was acquired at L- and X-band for different polarizations with the Canada Centre for Remote Sensing Convair CV-580 aircraft. The main objective of the present work is to explain the backscattering features visible in the SAR images in relation to in-situ data of surface topography and ice properties which were gathered on different ice islands and ice shelves. In order to aid the interpretation of the radar images, different theoretical models are used to simulate the scattering characteristics of various structural components of T-3.

2. DESCRIPTION OF RADAR IMAGES

In Figs. 1a-d different SAR images of T-3 are shown: an HH-polarized L-band image from SEASAT-A taken on October 3, 1978 (Fig. 1a), two images from the CV-580

4. now at Chalmers University of Technology, Department of Radio and Space Science, Göteborg, Sweden.

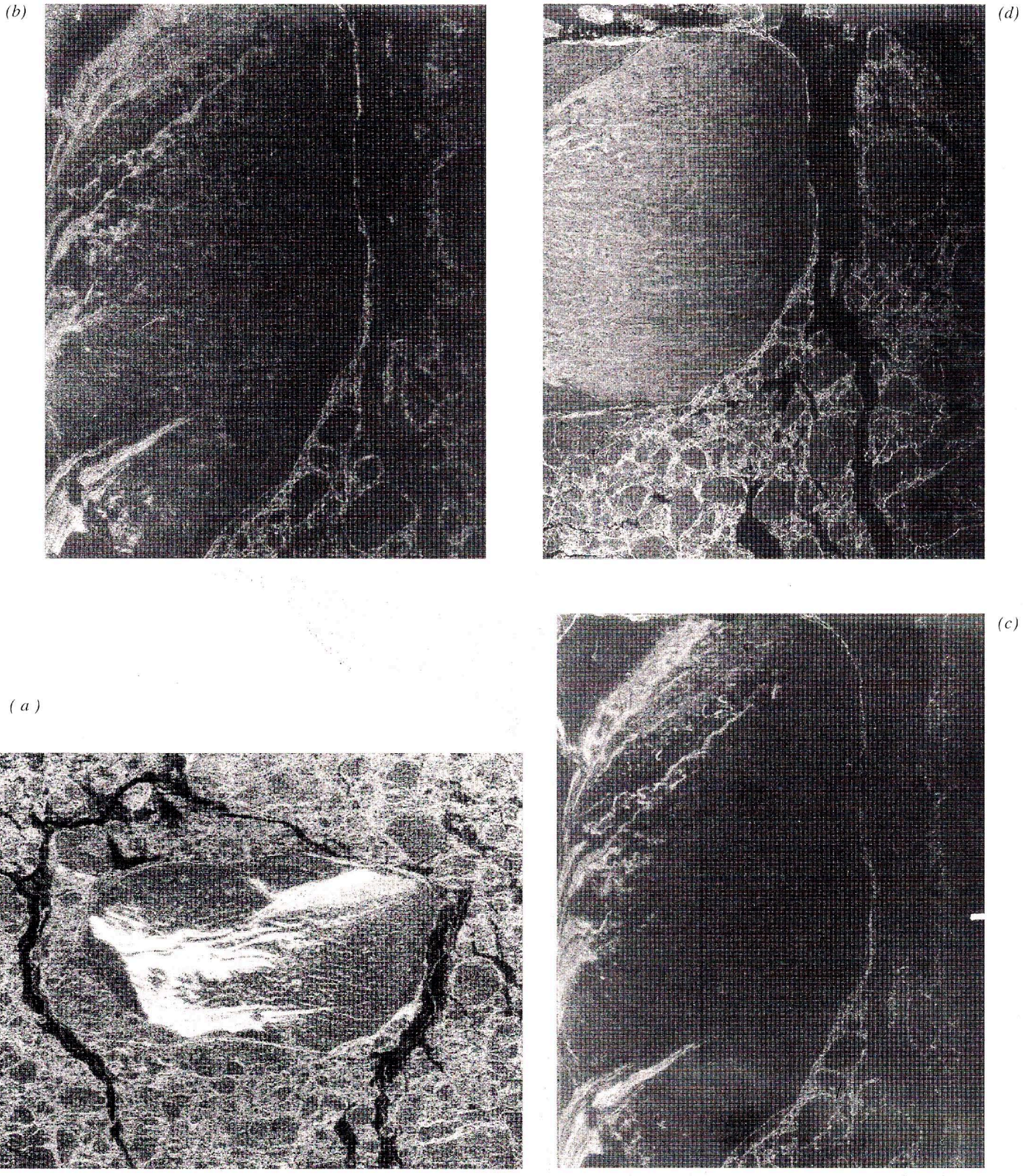

Fig. 1 - (a) SEASAT-SAR image of ice island T-3 taken on October 3, 1978. The radar frequency is 1.2 GHz (L-band), the polarization HH. (b) Airborne SAR image taken on March 16, 1979, at L-band (1.2 GHz) HH-polarization. (c) Airborne SAR image taken on March 16, 1979, at L-band HV-polarization. (d) Airborne SAR image taken on March 12, 1979, at X-band (9.3 GHz) HH-polarization.

aircraft taken on March 16, 1979 at L-band, HH- (Fig. 1b) and HV- (Fig. 1c) polarization, and a CV-580 aircraft HH-polarized X-band image from March 12, 1979 (Fig. 1d). The incidence angle of the SEASAT SAR was 23°, and the ground resolution 25 by 25 m. The illumination direction of the SEASAT SAR image is perpendicular to the long axis of T-3. The airborne images cover the sector across the lower third of T-3 in the SEASAT SAR image and are shown in slant range presentation with an image resolution of 3 m. The incidence angle ranges from nadir to 53°, and the illumination direction is parallel to the long axis of T-3.

The most striking features in both the co- and crosspolarization L-band images are stripes of strong returns which are spread irregularly over the island. Structural details and the partly meandering courses of single stripes are visible only at the fine resolution of the airborne SAR images. At the much coarser resolution of the SEASAT SAR image, the strong returns appear broader. Indications of a ribbed texture parallel to the long axis of the island can be seen in the HH-polarized images.

The X-band image of T-3 is characterized by a large area of narrow oblong returns, which are more distinct than those observed in the L-band images. They are primarily aligned parallel to the long axis of the island, but shorter stripes of strong backscattering are also oriented along other directions. Relative to the lineaments of strong returns, the average level of the backscattering intensity from areas between the lineaments is higher at X-band than at L-band. Patches of lower returns with a less distinct texture are visible near the edges of T-3. They correspond to the positions of multi-year ice floes which have been attached to the ice island. Large irregular patterns of strong returns similar to the ones observed at L-band are lacking in the X-band images.

3. SURFACE AND VOLUME STRUCTURE OF T-3

During the 50's and 60's several glaciological studies were carried out on T-3 which provided in-situ data of surface topography and volume structure. Certain data which are needed in modeling radar backscattering characteristics, however, were not measured on T-3. In such cases we refer to investigations of other ice islands or ice shelves.

In 1960 the upper portion of ice island T-3, down to a depth of about 8-16 m, was composed primarily of iced firn with a granular structure and many horizontal layers of air bubbles (Muguruma and Higuchi, 1963). Data of the air bubble size distribution are lacking from T-3. In the iced firn layer of Hobson's Choice Ice Island spherical bubbles of 0.1-3 mm in diameter and slightly elongated bubbles 2-3 mm in length with the long axis nearly normal to the ice surface were observed (Jeffries et al., 1991). Bodies of old lake ice were imbedded in the iced firn of T-3 (Smith, 1960). Lake ice bodies may contain vertical tubular air inclusions as much as 10-30 cm long in addition to much smaller spherical and elongated air bubbles (Ragle et al., 1964; Jeffries et al., 1991).

A heavy dirt layer was found in ice cores of T-3, separating the iced firn stratum from the basement ice below (Muguruma and Higuchi, 1963). The thickness of the heavy dirt layer was about 30 cm. The grain size was reported to be about 0.01 to 0.34 mm, the weight of dirt particles was 80 to 600 g/m^3 (Crary, 1958). Muguruma and Higuchi (1963) assumed a surface ablation rate of 0.5-1 m per year between 1952 and 1960. With this rate of surface ablation, parts of the dirt layer should have accumulated on the ice surface at the time of the radar overflights (1978, 1979). However, during the mid 70's no surface dirt was seen (Ramseier, personal communication).

The basement ice below the layer of heavy dirt consisted of four different strata. The uppermost stratum, which was about 2-3 m in thickness, was similar in composition to the iced firn, with inclined air bubble layers. Stratum II, about 10 m in thickness, showed a well developed stratification with a columnar texture and anisotropic structure (c-axis vertical). Stratum III and IV resembled sea ice and were each about 5 m in thickness. Below the basement a layer of sea ice was identified (Muguruma and Higuchi, 1963; Lyons et al., 1971). In sea ice the crystallographic c-axis has a preferred horizontal orientation (Golden and Ackley, 1981).

Holdsworth and Traetteberg (1974) measured depth profiles of ice density, salinity and temperature on T-3 for a 30 m deep drill hole during the spring of 1973. At depths between 23 m and 30 m they found slush ice, characterized by a salinity of more than 1 ppt. With a surface ablation rate of about 0.5 m per year the depth of this slush layer compares approximately with the depth of Muguruma's and Higuchi's strata III and IV in 1960. In the slush ice layers found on Hobson's Choice Ice Island Jeffries et al. (1991) observed spherical and elongated air inclusions, the latter 25-30 mm in length and oriented nearly normal to the ice surface. On Ward Hunt Ice Shelf

the air bubbles in saline ice were smaller and more numerous than those in glacier or lake ice, and the most frequent bubble shape was approximately teardrop (Ragle et al., 1964).

The surface of T-3 was covered by numerous broad, nearly parallel ridges and relatively narrow valleys, the latter being occupied by melt water lakes during the melt season. The ridge crests were typically 1-2 m and occasionally up to 5 m higher than the adjacent throughs. The distance between ridge crests on average was about 300 m. On this gentle undulating topography a second-order relief of smaller, more closely spaced ridges, valleys and mesa-like forms, as well as a third-order micro-relief of still smaller bumps and knobs were superimposed (Smith, 1960). The second-order ridges were formed by resistant old lake ice lenses which were exhumed by ablation. Mesa-like forms developed on modern lake ice pads. Similar surface morphologies were also observed on other ice islands (Jeffries and Sackinger, 1990).

Cracks up to 1 cm wide and a few meters long were seen on the surface of T-3 (Holdsworth and Traetteberg, 1974). Cracks may also form throughout the ice volume of ice islands, probably in the fall because of the rapid temperature drop, and endure several years before filling in (Legen'kov and Chugui, 1973). During the course of investigations of ice cores from Ward Hunt Ice Shelf fractures were observed to be common. Several of these fractures showed evidence of healing by planar orientation of air bubble sheets. Most of the fractures were a few centimeters in size with a subvertical orientation (Ragle et al., 1964).

4. DIELECTRIC CONSTANTS OF ICE TYPES AND ICE COMPONENTS OBSERVED ON T-3

The dielectric constant of either single ice components or of the ice-inclusion-mixture is needed in the scattering models. Because data of the dielectric properties of the different ice types observed on T-3 are not available, they are computed utilizing different empirical equations and theoretical models, as discussed in the following section.

4.1 Iced Firn

In our computations iced firn is modeled as a host medium of pure ice or slightly impure ice (salinity up to 0.03 ppt), throughout which spherical air bubbles are randomly distributed. Permittivity ε_h' and loss factor ε_h'' of the host medium are at a maximum, if temperature T, salinity S and density ρ are high, and at a minimum if the same parameters are low. We chose T=-5°C, S=0.03 ppt and ρ=0.9 g/cm^3 to calculate a dielectric maximum and T=-25°C, S=0 and ρ=0.7 g/cm^3 for the dielectric minimum. These values are based on the depth profiles of temperature, salinity and density given in Holdsworth and Traetteberg (1974). The low density value of 0.7 g/cm^3 is based on data given in Jeffries et al. (1991) for the iced firn surface of Hobson's Choice Ice Island, where melting along grain boundaries during previous summers had created a loose agglomeration of crystals.

Experimental data sets and empirical formulae relating the permittivity and loss factor of pure and slightly impure ice to temperature and salinity can be found in Mätzler and Wegmüller (1987). According to their results the dielectric constant of the host medium at a temperature of -5°C and a salinity of 0.03 ppt is ε_h= 3.18+j0.0048 at 1.2 GHz and ε_h= 3.18+j0.0033 at 9.3 GHz. In the case of pure ice values of ε_h=3.17+j0.00015 (1.2 GHz) and ε_h=3.17+j0.0005 (9.3 GHz) are obtained at a temperature of -25°C.

In order to include the scattering effects from a distribution of particles of different sizes, we evaluated the effective dielectric constant according to Ding and Tsang (1988), using a discretized Rayleigh size distribution with a mean air bubble size of 0.5 mm. An example is shown in Fig. 2 assuming an air volume fraction of 0.24 (for computational details see e.g. Tsang and Kong, 1992). In Table 1 the dielectric constants and the corresponding penetration depths are given for the selected maximum and minimum parameters. According to the calculated penetration depths given in Table 1, the radar returns at X-band are caused by scattering sources located in the upper firn layer of T-3, whereas the L-band waves penetrate much deeper and thus may also interact with structural inhomogeneities present in the basement of T-3.

Table 1 - Maximum and minimum dielectric constants of iced firn with corresponding penetration depths

Frequency:	1.2 GHz	9.3 GHz
Ice parameters:		
T=-5°C, S=0.03 ppt, ρ=0.9g/cm^3	3.13+j0.0047 / 15 m	3.13+j0.0032 / 2.6 m
T=-25°C, S=0 ppt, ρ=0.7g/cm^3	2.53+j0.0001 / 625 m	2.53+j0.0011 / 7.4 m

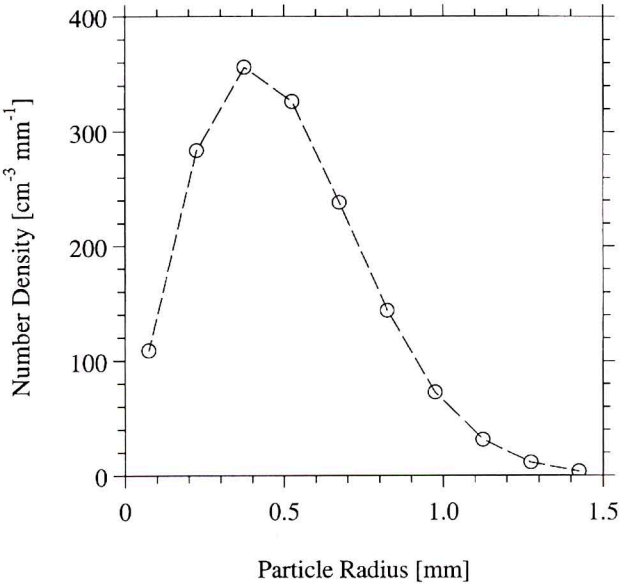

Fig. 2 - Number density of inclusion particles as a function of particle radius. In the model computations a Rayleigh size distribution with mean radius of 0.5 mm is discretized into 10 different equally spaced sizes, as indicated by the open circles. The distribution was calculated for a particle volume fraction of 0.24.

4.2 Heavy Dirt Layer

Petrographic studies of the dirt particles found on T-3 indicate that they are dusts of granites and gneisses (Muguruma and Higuchi, 1963) as well as of schists and volcanics (andesites, dacites and basalts) (Jeffries, personal communication). With a dirt weight of 600 g per m^3 of ice (Crary, 1958) and e.g. a density of 2.7 - 3.3 g/cm^3 (basalt) the dirt volume fraction is 0.00018-0.00022. Because of this very low particle concentration within the ice the changes in the dielectric constant of iced firn in the presence of dirt are negligible. The situation might be different if dirt particles accumulate on the ice surface due to ablation processes. If we assume e.g. a basaltic dirt accumulation with a volume fraction of 0.1, and a dielectric constant of 7.5+j0.4 which is based on measurements at 450 MHz and 35 GHz reported by Campbell and Ulrichs (1969), the dielectric constant of the dirt-ice mixture is ε_{dirt}=3.5+j0.02 compared to ε_{ice}=3.18+j0.002 of pure ice at L-band and X-band (T=-15°C, S=0.03 ppt, spherical dirt particles, scattering effects neglected). The effect of surface dirt, however, is of minor importance with regard to the radar signature analysis of ice island T-3.

4.3 Saline Ice Layers

The lowermost layers of T-3 are characterized by their high salt content. Holdsworth and Traetteberg (1974) reported maximum values of more than 1.1 ppt in depths larger than 24 m. Because of this large depth the saline layers have to be considered only with regard to the L-band radar signatures of T-3. The dielectric constant of a saline layer depends on the shape and orientation of the brine inclusions. From investigations of the ice island ARLIS II, which mainly consisted of basement ice, it is known that the saline ice is characterized by locally aligned crystals. The areas of alignment are as large as 10 m (Smith, 1964). According to Golden and Ackley (1981) the long axes of the brine ellipsoids are oriented horizontal, and they are perpendicular to the crystal c-axes. In order to evaluate the dielectric tensor of the saline ice layer we applied the Polder-Van Santen / de Loor formula (Ulaby et al., 1986, pp. 2030-2040). The volume fractions of brine and air are calculated according to Cox and Weeks (1983), and the dielectric constant of brine according to Stogryn and Desargant (1985). For the reason of computational ease we approximate the brine inclusions by prolate (needle shaped) spheroids. We assume c=3 mm and a=b=0.25 mm as the dimensions of the spheroid axes with the c-axes all parallel aligned in the horizontal plane (corresponding to the direction of the optical axis). These values are based on data given in Golden and Ackley (1981) and in Ragle et al. (1964). For a temperature of -3°C, a density of 0.91 g/cm^3 and a salinity of 1.1 ppt the components of the dielectric tensor are ε_c=4.18 +j0.61 and ε_a=ε_b=3.25+j0.005. If scattering losses are ignored, the penetration depths of the extraordinary wave (electric field vector parallel to the optical axis) and ordinary wave (electric field vector perpendicular to the optical axis) are 0.13 m and 14.6 m, respectively. Examples of penetration depths for slight changes in the spheroid dimensions are 0.3 m and 13.8 m, if c=3 mm and a=b=0.5 mm (ε_c= 3.25+j0.005 and ε_a=3.87+j0.25) and 0.2 m and 14.3 m, if c=2 mm and a=b=0.25 mm (ε_c=3.24+j0.005 and ε_a= 4.02+j0.39).

5. SURFACE SCATTERING

The intensity of the e.m. field scattered by a plane ice surface depends on the dielectric constant of the ice, the surface roughness in the mm-dm range ("small-scale roughness"), the radar frequency and the radar incidence angle. The small-scale surface roughness is parameterized by the surface height standard deviation (rms-height) σ_z, the surface correlation length l_z and the type of surface correlation function. In the following section we assume that the variations in the small-scale surface elevation are statistically independent of the azimuth angle and that the surface correlation function can be approximated by an exponential function. The radar incidence angle is measured relative to the vertical.

Theoretical models which have found a wide application in modeling surface backscattering are the Kirchhoff Model (KM) and the Small Perturbation Theory (SPM) (Ulaby et al., 1982, chapter 12). These models, however, are restricted to certain ranges of surface roughness and radar incidence angles. In-situ small-scale roughness data of ice island T-3 are not available. In our computations we used σ_z= 0.2 cm / l_z=10 cm for a smooth surface, and σ_z=0.8 cm / l_z=5 cm for a rough surface, respectively. A similar range is covered by Arctic multi-year sea ice. At X-band these roughness parameters are within the validity range of the Physical Optics (PO) Approximation of the Kirchhoff Model, at L-Band the first order SPM is valid. Both models can be applied if the variations of the radar incidence angle lie within the interval [20°,70°]. We took a dielectric constant of 2.98+j0.0022 at L-band and 2.98+j0.0029 at X-band (T=-15°C, S=0.03 ppt, ρ=0.85 g/cm^3 and a Rayleigh size distribution with r_{mean}=0.5mm).

The surface relief of T-3 as described by Smith (1960) consists of ridges, valleys and mesa-like structures ("large-scale roughness"). We assume that the relief can be approximated by planar facets tangential to the ice surface, and that the dimensions of the facets are much larger than the radar wave length. The facets are covered by undulations in the mm - dm range which represent the small-scale surface roughness. The backscattering intensity thus depends on the local incidence angle of the radar beam on the facets, which is measured relative to the facet normal, and on the small-scale roughness of the facet surface. We ignore diffraction effects caused by sharp edges ("sharp" relative to the radar wave length).

In Fig. 3 the backscattering coefficient σ°, which is a measure of the backscattered intensity, is shown as a function of the local incidence angle for a smooth and a rough facet surface. The polarization of the radar waves is HH (both transmitted and received radar signal are linear polarized in the horizontal plane). Within the local incidence angle interval 20° to 70°, the intensity of the backscattered radar waves decreases by 18-20 dB. The difference between the smooth and the rough surface is 10-12 dB. At L-band the backscattering coefficient is 10-15 dB lower than the corresponding value at X-band, because a certain surface appears smoother to the long L-band waves and rougher to the short X-band waves. In the case of backscattering both the KM-PO and first-order SPM yield a cross-polarized return of zero. If we use the minimum and maximum dielectric constants given in Table 1, σ° is 0.4 dB larger for ε at the maximum and 1.3 dB smaller for ε at the minimum compared to the results depicted in Fig. 3.

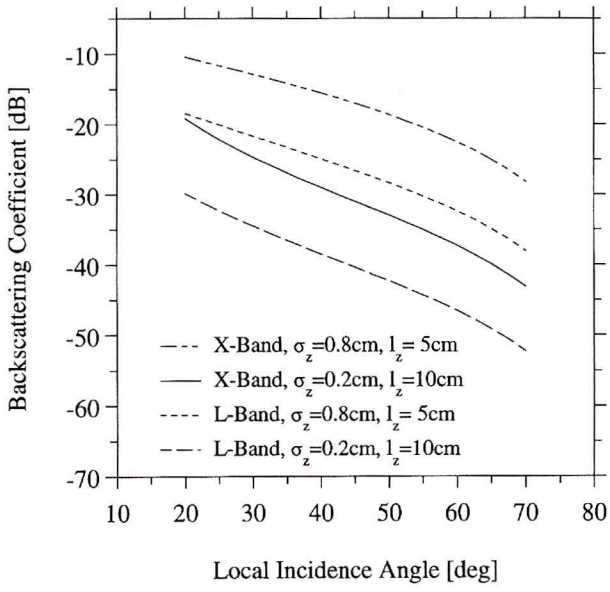

Fig. 3 - Theoretical surface backscattering coefficient of planar facets as a function of the local incidence angle at X- and L-band. The polarization is HH (the cross-polarized return is zero). Curves are shown for a rough (σ_z=0.8 cm, l_z=5 cm) and a smooth (σ_z=0.2 cm, l_z=10 cm) facet surface.

Because of the almost parallel alignment of many of the ridge axes on T-3, the surface scattering characteristic depends on the island's orientation relative to the radar look direction. Variations of the local incidence angle are largest if the ridge axes are oriented normal to the radar look direction, and at a minimum if the ridge axes are parallel to the illumination direction. This item is depicted in Figs. 4a-4b for different radar incidence angles. We considered a tilt angle variation of the surface facets which ranges from -30° to +30°.

For the case of perpendicular orientation the local incidence angle varies from -15° to +45° at a radar incidence angle of 15°, and from 15° to 75° at a radar incidence angle of 45° (Fig. 4a). Here we assumed that the facet normal lies in the plane of incidence. Note that the facet tilt is given relative to the horizontal, and that a negative value of the tilt angle corresponds to a facet facing the radar. Negative local incidence angles only occur on facets facing the radar, indicating that the angle between facet normal and the vertical is larger than the radar incidence angle. The backscattering coefficient, however, depends on the absolute value of the local incidence angle. The backscattered intensities of surface facets with different tilts, but the same absolute local incidence angles, are thus equal. A local incidence angle of 0° corresponds to specular reflection. If the radar incidence angle is near grazing, facets facing away from the radar might be located in the shadow of the radar illumination. In summary, variations of the radar signal backscattered from the surface will be largest at low values of

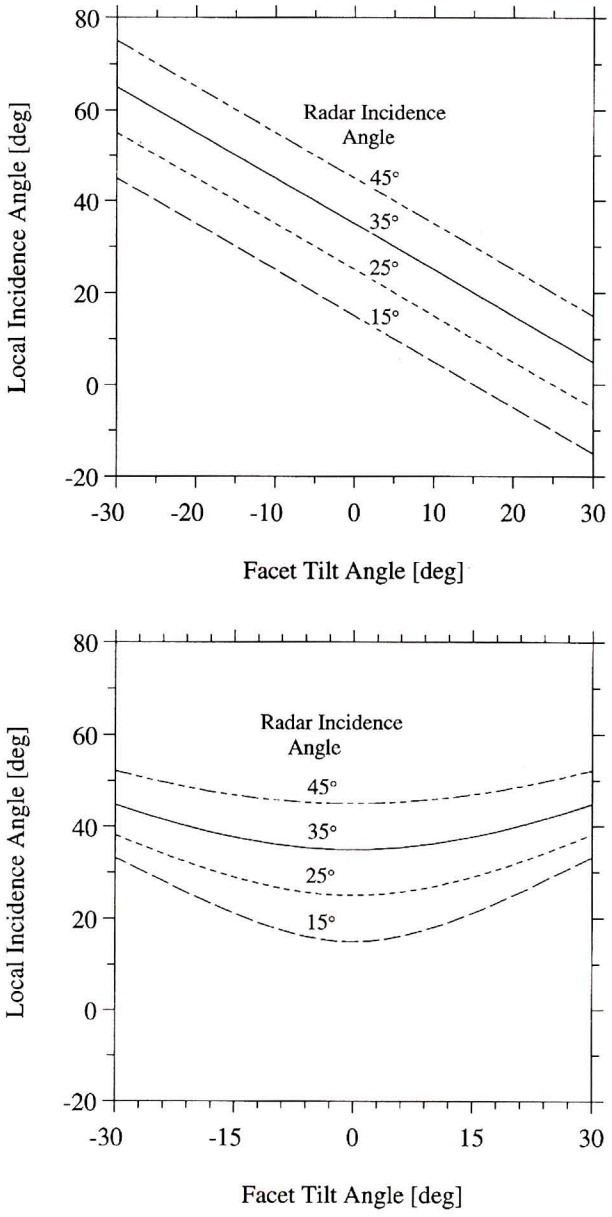

Fig. 4 - Local incidence angle as a function of the facet tilt angle if the radar look direction is perpendicular (a) and parallel (b) to the axes of ridges and valleys observed on the surface of T-3. Curves are shown for different radar incidence angles.

the radar incidence angle because the backscattering coefficient is much larger than the noise level of the radar receiver and because of possible contributions from specular reflections. The amplitude of the σ^o-variations for a particular range of local incidence angles within the interval [20°,70°] can be found from Fig. 3.

In the computations which Fig. 4b is based on it is assumed that the ridge axes are oriented parallel to the radar look direction, and that the facet normals lie in a plane perpendicular to the plane of incidence. Compared to Fig. 4a the variations of local incidence angles are much less, and the variation range decreases with increasing radar incidence angle. The lowest value of the local incidence angle is identical to the radar incidence angle, specular reflections will not occur for the range of radar incidence angles given in Fig. 4b. If a ridge is symmetric in cross section, the radar signatures are identical for both sides of the ridge. The variations of the surface scattering contribution will be significantly smaller than the ones observed in the case of ridges oriented perpendicular to the radar look direction. Although the backscattering coefficients have to be calculated in a "two scale" model if illumination direction and ridge axes are parallel (because the normal of the scattering facet does not lie in the plane of incidence), the results of Fig. 3 can be used as a good approximation (Ulaby et al., 1982, chapter 12, pp. 966-973).

6. VOLUME SCATTERING

6.1 Iced Firn

The radar waves which are transmitted into the iced firn are scattered by the air bubbles within the ice. The intensity of volume scattering depends on volume fraction, size, dielectric properties, shape and orientation of inclusion particles imbedded in the host medium. From the variety of models focusing on volume scattering we selected the Dense Medium Radiative Transfer Method (DMRT), which is described e.g. in Wen et al. (1990). In this model discrete scatterers are imbedded in a homogeneous host medium. Multiple scattering, absorption, and interferences of the e.m. fields scattered from different particles are included.

In our model simulations we considered a slab of iced firn, consisting of densely distributed spherical air bubbles imbedded in a background of pure or slightly impure ice. The slab is overlying a homogeneous half space of slightly impure ice. The air bubble size distribution of our model is shown in Fig. 2. The inclusion radii are within the regime of Rayleigh scattering. The small-scale surface roughness of the iced firn is neglected.

In order to calculate the dielectric properties we assume the following parameters based on the depth profiles reported in Holdsworth and Traetteberg (1974): T=-15°C, S=0.03 ppt, ρ=0.85 g/cm^3 for the host medium of the scattering slab (thickness 8 m) and T=-5°C, S=0.03 ppt, ρ=0.91 g/cm^3 for the lower half space. The resulting dielectric constants are listed in Table 2. The volume backscattering coefficient for the given parameters is shown in Fig. 5 as a function of the incidence angle.

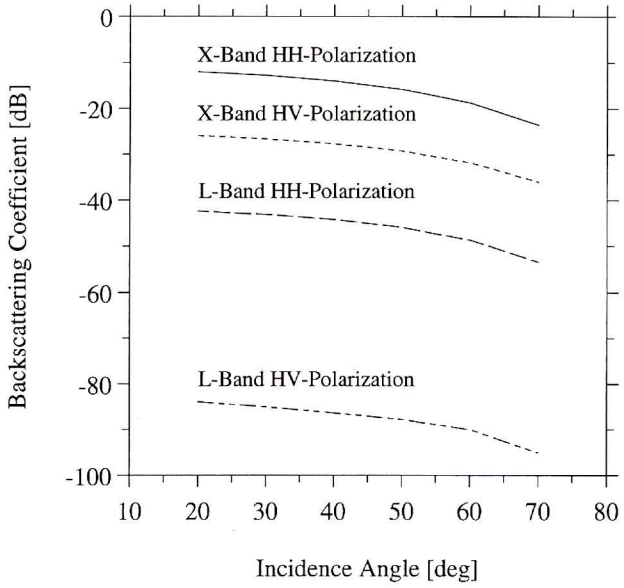

Fig. 5 - Theoretical volume backscattering coefficient of iced firn as a function of incidence angle. The density of the iced firn is 0.85 g/cm³, the firn layer thickness 8 m. The air bubble size distribution is a discretized Rayleigh function with an average radius of 0.5 mm.

Compared to the results of the surface scattering simulations presented in Fig. 3, volume scattering is negligible at L-band. At X-band, however, the intensity level of volume scattering at HH-polarization is nearly equal to the surface scattering contribution in the case of the rough surface and even larger in the case of the smooth ice surface. The decrease of the backscattering coefficient with increasing incidence angle is less than in the case of surface scattering.

In Fig. 6 the volume backscattering contribution is shown as a function of the layer thickness for an incidence angle of 35°. At larger layer thicknesses (> 5 m) the increase of the backscattering coefficient is negligible at X-band. This is due to absorption and scattering losses in the upper portions of the iced firn.

6.2 Lake Ice, Cracks and Fractures

In order to simulate the scattering characteristics of the tubular air inclusions found in lake ice as well as of fractures and cracks we used the Radiative Transfer Method for ellipsoidal scatterers in a first-order approximation according to Tsang et al. (1981). This approach is limited to the low-frequency (Rayleigh) regime where all particle dimensions are small compared to the radar wave length. Therefore we restricted our model computations to L-band and neglected the influence of large air voids.

Table 2 - Dielectric properties needed in the volume scattering simulations shown in Figs. 5 and 6. The dielectric constants of pure and slightly impure ice were evaluated according to Mätzler and Wegmüller (1987).

	scattering layer (iced firn)	lower half space (slightly saline ice)
temperature	-15°C	-5°C
salinity	0.03 ppt	0.03 ppt
density	0.85 g/cm³	0.91 g/cm³
dielec. const. L-band host medium)	(3.17+j0.0024	
dielec. const. X-band (host medium)	3.17+j0.0022	
dielec.const. L-band (mixture)	2.98+j0.0021	3.16+j0.0048
dielec. const. X-band (mixture)	2.98+j0.0027	3.16+j0.0033

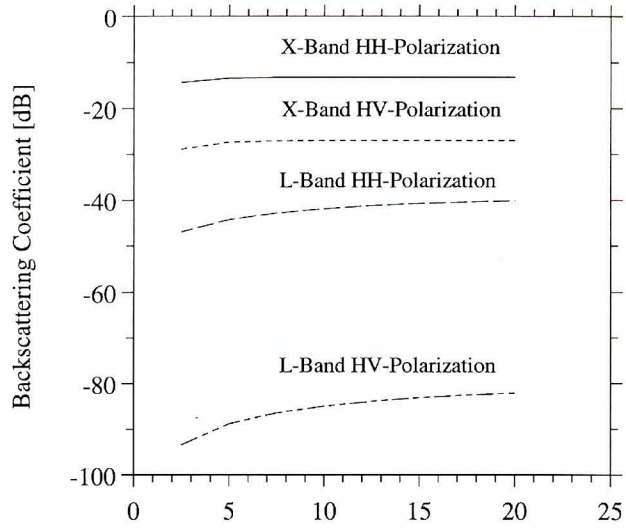

Fig. 6 - Theoretical volume backscattering coefficient of iced firn as a function of layer thickness. The radar incidence angle is 35 degrees, the firn density 0.85 g/cm³. The air bubble size distribution is a discretized Rayleigh function with an average radius of 0.5 mm.

Moreover, the model is based on the assumption of a low volume fraction of scattering particles so that the correlation of scatterer positions can be ignored. The first order appproximation accounts only for single scattering events.

Our model consists of a slab of air filled ellipsoids imbedded in a homogeneous background of slightly impure ice (dielectric constant of the host medium is 3.17+j0.0024). The thickness of the slab is 10 m. Small cracks and tubu-

lar air inclusions as observed in lake-ice lenses are approximated by prolate ("needle-shaped") spheroids, fractures by oblate ("disk-shaped") spheroids. The spheroids are randomly oriented in azimuth, the tilt-angle distribution is assumed to cover a narrow range of ±5° around the vertical and the horizontal, respectively, i.e. all spheroids are inclined either nearly vertically or nearly horizontally. The ellipsoid axes are indicated as a, b, c with c>a and a=b for a prolate spheroid and c<a, a=b for an oblate spheroid. The c-axis is the axis of symmetry.

The effect of the inclusion shape on the backscattering coefficient is depicted in Fig. 7 as a function of the long spheroid axis (i.e. 'c' for a prolate spheroid, and 'a' for an oblate spheroid). The spheroid volume is kept constant and equals the volume of a sphere with radius 10 mm (oblate spheroid) and 6.3 mm (prolate spheroid), respectively. Compared to the volume of oblate spheroids, the volume of prolate spheroids was chosen smaller by a factor of 4 to give a closer approximation to the oblong shape of tubular air inclusions and cracks. The backscattering coefficients of spherical scatterers with the given radii are also depicted for co-polarization in Fig. 7. The cross-polarization return of spherical scatterers is a second-order effect and thus is zero in the first-order approximation used here. As can be seen from Fig. 7, the backscattering coefficient of vertical aligned prolate spheroids and of oblate spheroids with horizontal axes of symmetry is slightly larger than σ° of a sphere of the same volume and increases with increasing eccentricity. Here the symmetry axes of the oblate spheroids are oriented randomly in the horizontal plane. The backscattering coefficient is smaller in the case of horizontally inclined prolate spheroids and oblate spheroids with vertical axes of symmetry and decreases with increasing eccentricity. Here the long axes of the needle-shaped prolate spheroids are oriented randomly in the horizontal plane. The cross-polarized returns are largest for oblate spheroids with randomly oriented horizontal axes of symmetry and smallest for vertically aligned prolate spheroids. In Figs. 8 and 9 the backscattering coefficients of prolate spheroids with c=25 mm and a=3.2 mm and of oblate spheroids with a=25 mm and c=1.6 mm are depicted as functions of volume fraction and radar incidence angle. Note that for the given dielectric constants of the host medium and the inclusions, the maximum radius of a spherical scatterer within the Rayleigh regime is 19 mm at L-band. The decrease of σ° with increasing incidence angle usually is only slight up to 50 degrees, σ°_{HV} of vertical aligned prolate spheroids and of oblate spheroids with vertical axes of symmetry, however, increases with increasing incidence angle in the range from 0 to 50 degrees.

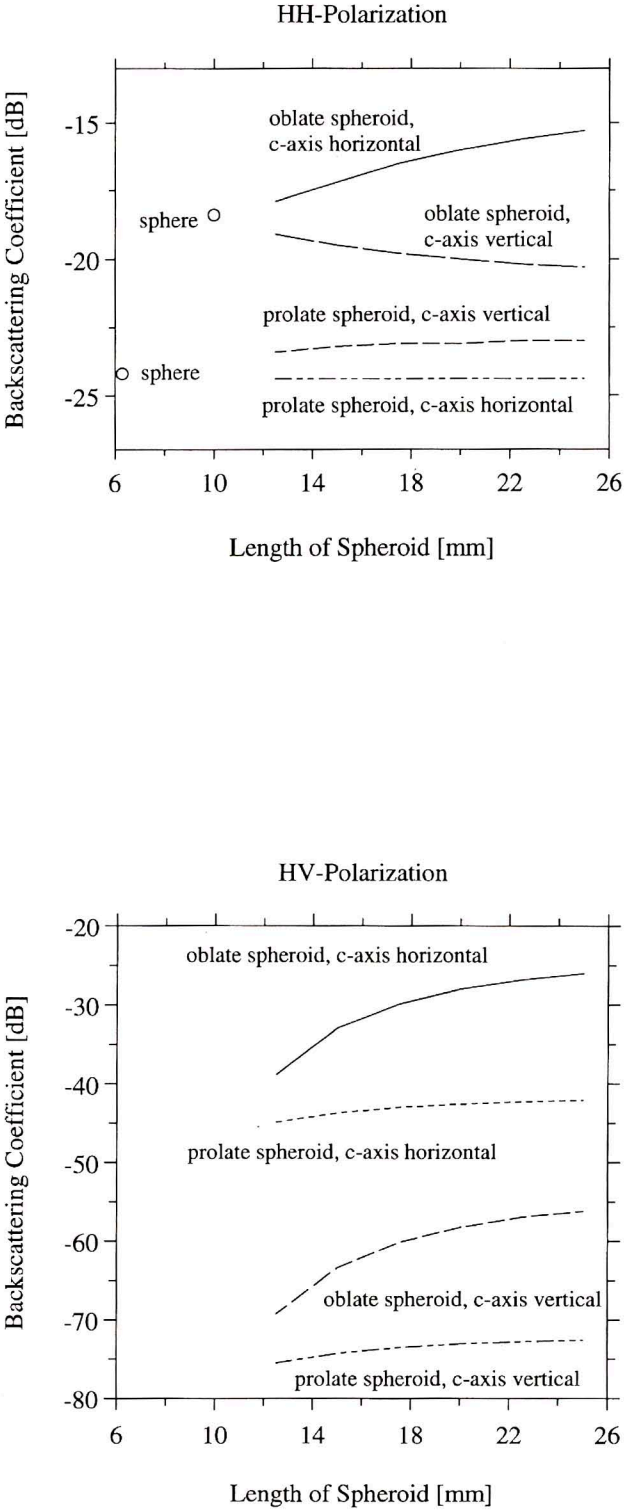

Fig. 7 - Theoretical volume backscattering coefficient of ellipsoidal particles at L-band as a function of maximum ellipsoid dimension. The air filled scattering particles are either oblate (disk-shaped) spheroids (axes a=b, c<<a) or prolate (needle-shaped) spheroids (axes a=b, c>>a). The volume of the oblate spheroids is equal to a sphere 20 mm in diameter, the volume of the prolate spheroids equals the volume of a sphere 12.6 mm in diameter. The radar incidence angle is 30 degrees, the scatterer volume fraction 0.005, and the layer depth 10 m.

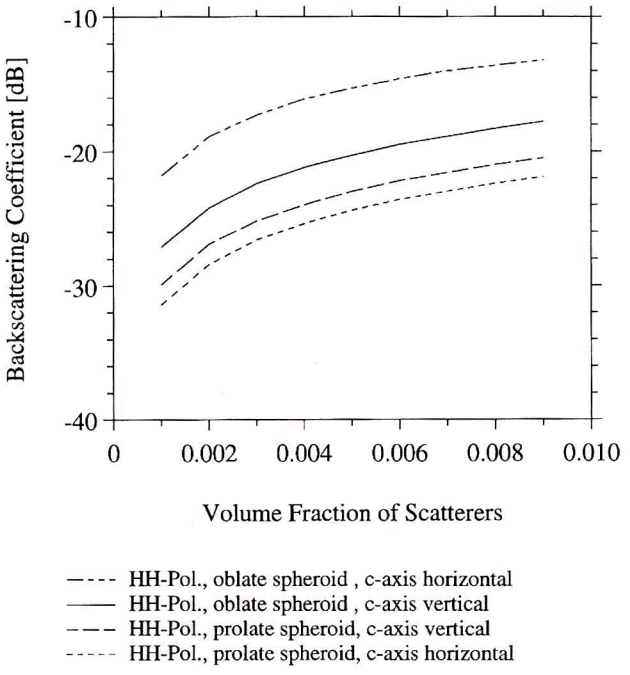

Fig. 8 - Theoretical volume backscattering coefficient of ellipsoidal particles at L-band as a function of volume fraction. The axes of oblate spheroids are a=b=25 mm, c=1.6 mm, the axes of prolate spheroids are a=b=3.2 mm, c=25 mm. The radar incidence angle is 30 degrees.

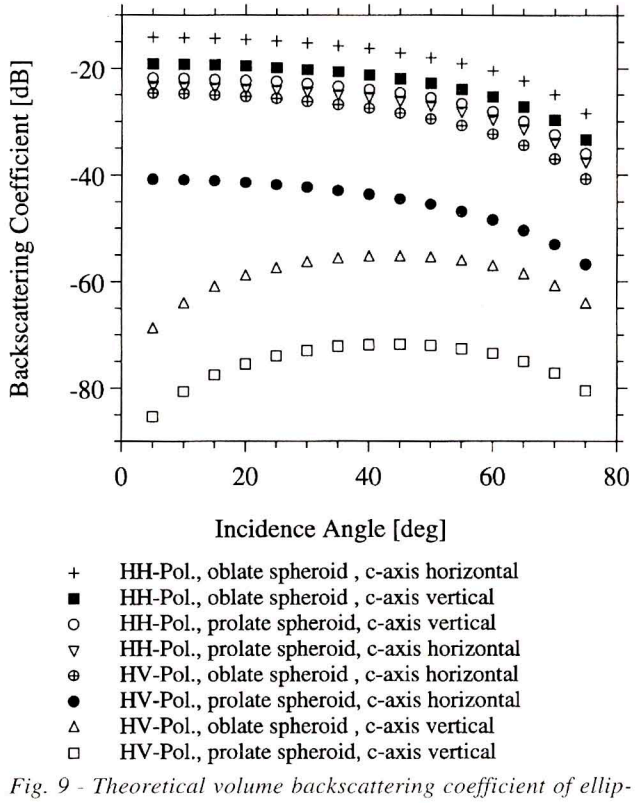

Fig. 9 - Theoretical volume backscattering coefficient of ellipsoidal particles at L-band as a function of incidence angle. The axes of oblate spheroids are a=b=25 mm, c=1.6 mm, the axes of prolate spheroids are a=b=3.2 mm, c=25 mm. The volume fraction of scatterers is 0.005.

7. DISCUSSION AND CONCLUSIONS: INTERPRETATION OF RADAR SIGNATURES OF T-3

In the preceding sections we summarized surface observations and results of physical-structural ice property investigations made on T-3 and other ice islands or ice shelves as far as they are important in interpretation of the microwave signatures observed in the SAR images of T-3. Based on in-situ data, results of surface and volume scattering models were presented, which will aid the analysis of the radar signature features in the following sections.

7.1 Ribbed Texture

A significant backscattering characteristic observed in the SAR images of ice shelves and ice islands is a ribbed texture. Jeffries and Sackinger (1990), who analysed X-band SAR data, stated that this type of texture results from the quasi-periodic surface undulations of ice islands, which are identical to the first-order relief observed on T-3 (Smith, 1960). The ribbed texture is particularly evident if the radar look direction is perpendicular to the crest and trough axes on the ice island. In this case the variations of the local incidence angle are largest as was discussed in section 5 (Fig. 4a). If the axes of crests and troughs are parallel to the radar look direction as in Fig. 1d, the local incidence angles are less variable (Fig. 4b), and the texture is less distinctive, but clearly visible.

In order to explain the scattering mechanism causing the ribbed texture, we approximated the shape of the island's surface by plane facets, and assumed that the facets are covered by small-scale undulations in the mm-dm range. The intensity of the signal backscattered to the radar depends on the small-scale roughness and on the tilt angle of the facets. Because on one hand the surface-tilt variations due to the first-order relief as defined by Smith (1960) are very low, and on the other hand the facets at X-band are relatively small and follow the height variations of the island's surface fairly well, we assume that the image texture at X-band is mainly caused by surface scattering from the second-order relief of the ice island. At L-band the surface scattering intensity is much lower (Fig. 3). Because the L-band waves are about 8 times the length of the X-band waves, the surface-facets at L-band cover a relatively larger area, and variations in the local incidence angle over short distances are averaged in the radar image. The contribution of surface scattering to the image texture at L-band has to be considered, if the radar look direction

is perpendicular to the ridge axes as in Fig. 1a, but it is of minor importance, if the radar look direction is parallel to the ridge axes as in Figs. 1b and 1c

Relative to the lineaments of strong returns, the average level of the backscattering intensity from areas between the lineaments is higher at X-band than at L-band. This can be explained by volume scattering processes within the air bubble layers found in the ice (Fig. 5). Another source of strong volume scattering are the bodies of lake ice imbedded in the iced firn because they contain tubular air inclusions up to a few centimeters in size. At X-band most of the inclusions are large enough to cause diffraction and multiple reflections. However, the magnitude of intensity reflected back to the radar is difficult to predict theoretically because the reflection and diffraction processes within an assemblage of tubular air inclusions are rather complex. Several ridges and mesa-like structures observed on T-3 were formed by lake ice lenses (Smith, 1960), therefore the ribbed texture is most probably enhanced in X-band images by scattering processes in the lake ice.

Volume scattering from lake ice lenses may also cause the indications of surface undulations which are visible in the L-band HH-polarized image Fig. 1b. A ribbed texture is not observed in the L-band cross-polarization image (Fig. 1c). According to the volume scattering simulations presented in section 6, the vertical aligned air inclusions in lake ice are characterized by a low depolarization return.

7.2 Irregular Strong Returns

Both the co- and cross-polarized L-band images are characterized by the appearance of the same strong radar returns (Figs. 1b and 1c). This can be explained by the presence of regions containing nonspherical scattering elements. As was mentioned in section 3, Ragle et al. (1960) observed fractures to be common in ice cores from Ward Hunt Ice Shelf. Although the fractures were healed, they could be identified either by the formation of new crystal assemblages of textures different from the adjacent grains or by the formation of planar sheets of bubbles marking a "ghost fracture". Most of the fractures were subvertical, and only a few of them had a dip less than 45 degrees.

In our volume scattering simulations in section 6 we approximated the ghost fractures by homogeneous air filled oblate spheroids. Applying this approximation, we assume that the reduction in the dielectric contrast which occurs if the scattering body is formed by an accumulation of air bubbles is only slight, and we neglect interactions of the electromagnetic fields scattered from individual air bubbles. The depolarization return is strongest if oblate (disk-shaped) spheroids with horizontal axes of symmetry are oriented randomly in azimuth (Figs. 7 and 8). In this case the magnitude of σ°_{HV} is comparable to the L-band surface scattering contribution (Fig. 3) and the L-band volume scattering contribution from the iced firn (Figs. 5 and 6), although the volume scattering simulations for nonspherical particles were restricted to a sparsely distribution of size limited scatterers. We conclude that the stripes of strong radar returns may be caused primarily by regions of subvertical fractures and possibly also by accumulations of cracks. The regions of fractures and cracks are located in the basement ice of T-3 and thus are not imaged by the X-band radar because of its smaller penetration depth. Because of the magnitude of σ°_{HV} the fractures and cracks are at least a few centimeters in size.

An assumption inherent in the fracture region hypothesis is that the depolarization of the incident wave is caused by the nonspherical shape of scattering particles, which are imbedded in an isotropic host medium. However, depolarization can also occur in anisotropic host media, as e.g. in saline layers, which have been found in the lowermost portion of T-3. In the following discussion we assume that the optical axis of an uniaxial anisotropic layer is parallel to the x-axis of a Cartesian coordinate system. The radar waves are horizontally polarized and propagate in the z-direction. The electric field vector is aligned at an angle ϕ with the x-axis (Fig. 10). When a linearly polarized wave penetrates into the uniaxial anisotropic layer, it is separated into two components with their electric field vectors along the x-axis (extraordinary wave) and y-axis (ordinary wave). The electric fields are (see Fig. 10)

$$E_x(z,t) = E_{oh}\cos\phi \exp(-\kappa_x z/2) \cos(2\pi ft+k_x z)$$

and

$$E_y(z,t) = E_{oh}\sin\phi \exp(-\kappa_y z/2) \cos(2\pi ft+k_y z)$$

where subscript h indicates horizontal polarization, κ is the extinction coefficient, k the wave number, and f the frequency. Because propagation velocity and extinction coefficient are different for the ordinary and extraordinary wave component, the resulting wave is elliptically polarized. The components at horizontal and vertical polarization are (Fig. 10):

$$E_h(z,t) = E_x(z,t)\cos\phi + E_y(z,t)\sin\phi$$

and

$$E_v(z,t) = -E_x(z,t)\sin\phi + E_y(z,t)\cos\phi$$

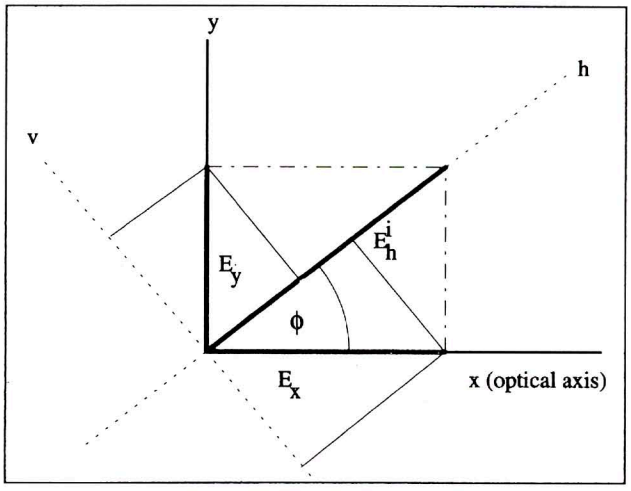

Fig. 10 - Components of the electric field vector in an uniaxial anistropic medium. The optical axis is parallel to the x-axis, the e.m. wave propagates in z-direction, "v" is the direction of vertical polarization, "h" the direction of horizontal polarization.

They dependent on the azimuth angle ϕ and the distance the wave has travelled through the anisotropic medium.

According to our results discussed in section 4, the ordinary and extraordinary waves are absorbed in very different proportions ($\kappa_x >> \kappa_y$). After a few meters the extraordinary wave is almost completely absorbed, and the wave propagating through the saline layer becomes linearly polarized in the y-direction. Thus the horizontally and vertically polarized intensities can be approximated as

$$I_h \sim E_{oh}^2 \exp(-\kappa_y z) \sin^4\phi$$

and

$$I_v \sim E_{oh}^2 \exp(-\kappa_y z) \cos^2\phi \sin^2\phi$$

In order to give an estimate of the magnitude of intensity transferred from the incident horizontal polarized wave into the vertical polarized component, we evaluate the average intensity components over ϕ, i.e. we assume that the orientation of the optical axis is equally distributed between $0 \le \phi \le \pi$ within a sufficiently large area:

$$\langle I_h \rangle_\phi \sim 0.375\, E_{oh} \exp(-\kappa_y z)$$

and

$$\langle I_v \rangle_\phi \sim 0.125\, E_{oh} \exp(-\kappa_y z)$$

i.e. on the average one third of the intensity is polarized vertically after the incident wave has propagated through the anisotropic layer.

The saline layers are characterized by areas of local anisotropy, which are a few meters in size (Smith, 1964). On a scale of a few hundred meters the orientation of the optical axes is variable. The magnitude of depolarization depends on the angle ϕ between the radar look direction and the optical axis, it is largest if ϕ=45 or ϕ=135 degrees and zero if ϕ=0, 90 or 180 degrees. If the radar signal is scattered e.g. by the nearly spherical air inclusions imbedded in a sea ice layer or by the vertically aligned elongated air inclusions observed in slush ice, it will appear as speckle-like noise in the cross-polarized image, as it is observed between the stripes of strong returns in the L-band HV-polarized image (Fig. 1c). We assume that scattering contributions which have been depolarized by traversing the saline layers are of minor importance.

7.3 Conclusions

In this paper different scattering models have been utilzed to simulate the radar signature characteristics of structural components observed on T-3, other ice islands and ice shelves. The results indicate that:

- the ribbed texture observed in the X-band HH-polarization radar image of T-3 (Fig. 1d) is caused both by surface scattering contributions from the second-order surface topography and by volume scattering contributions from long parallel ridges underlain by lake ice lenses.
- if the radar look direction is parallel to the long axis of T-3, volume scattering from ridges consisting of lake ice is the dominant source of the ribbed texture at L-band HH-polarization (Fig. 1b), whereas surface scattering is of minor importance. If the radar look direction is perpendicular to the long axis of T-3 (Fig. 1a), contributions from both volume and surface scattering have to be considered.
- the mean scattering intensity between lineaments of stronger returns observed in the X-band image (Fig. 1d) is due to scattering processes within the air bubble layers present in the iced firn.
- the strong radar returns which are apparent in both the L-band HH- and HV-polarization images of T-3 (Figs. 1b and 1c) can be explained by assemblages of mainly subvertical fractures of a few centimeters in size. We assume that these fracture zones were located in the basement ice of T-3.

ACKNOWLEDGEMENTS

We thank Peter Lemke (Alfred-Wegener-Institute, Bremerhaven, Germany) for his comments made on the manuscript. We express our gratitude to Martin Jeffries (University of Alaska, Fairbanks) for providing us with

lots of information about the structure and ice properties of ice islands. We like to thank the Canadian Centre for Remote Sensing for the CV-580 images and the Jet Propulsion Laboratory for the SEASAT SAR image. Finally special thanks go to Barbara Burns for suggesting the collaboration between the authors and inspiring the work. This is Contribution 861 from the Alfred-Wegener-Institute.

REFERENCES

Campbell M.J. & Ulrichs J., 1969, Electrical Properties of Rocks and Their Significance for Lunar Radar Observations, J. Geophys. Res. 74, pp.5867-5881.

Cox G.N.F. & Weeks W.F., 1983, Equations for Determining the Gas and Brine Volumes in Sea Ice Samples, J. Glaciology, Vol. 29, No 102, pp. 306-316.

Crary A.P., 1958, Arctic Ice Island and Ice Shelf Studies : Part I, Arctic 11, No 1.

Ding K.H. & Tsang L., 1988, Effective Propagation Constants of Dense Nontenuous Media with Multi-Species of Particles, J. Electromagn. Waves and Applications, Vol. 2, No 8, pp. 757-777.

Golden K.M.& Ackley S.F., 1981, Modeling of Anisotropic Electromagnetic Reflection from Sea Ice, J. Geophys. Res., Vol. 86, No C9, pp. 8107-8116.

Holdsworth G. & Traetteberg A., 1974, The Deformation of an Arctic Ice Island, Second International Conference on Port and Engineering under Arctic Conditions, University of Iceland, Dept. of Engineering and Science.

Jeffries M.O.& Sackinger W.M., 1990, Ice Island Detection and Characterization With Airborne Synthetic Aperture Radar, J. Geophys. Res., Vol. 95, No C4, pp. 5371-5377.

Jeffries M.O., Serson H.V., Krouse H.R. & Sackinger W.M., 1991, Ice Physical Properties, Structural Characteristics and Stratigraphy in Hobson's Choice Ice Island and Implications for the Growth History of East Ward Hunt Ice Shelf, Canadian High Arctic, J. Glaciology, Vol. 37, No 126, pp. 247-260.

Jeffries M.O., 1992, Arctic Ice Shelves and Ice Islands: Origin, Growth and Disintegration, Physical Characteristics, Structural-Stratigraphic Variability, and Dynamics, Reviews of Geophysics, 30, 3, pp. 245-267.

Legen'kov A.P.& Chugui I.V., 1973, Results of Morphometric Measurements of the Ice Island of the Severnyi Polyus-19 Drifting Station, Problemy Arktiki i Antarktiki, Vol. 42, pp. 44-48.

Lyons J. B., Savin S.M.& Tamburi A J., 1971, Basement Ice, Ward Hunt Ice Shelf, Ellesmere Island, Canada, J. Glaciology, Vol. 10, No 58.

Mätzler C. & Wegmüller U., 1987, Dielectric Properties of Fresh Water Ice at Microwave Frequencies, J. Phys. D: Appl. Phys. 20, pp. 1623-1630.

Muguruma J. & Higuchi K., 1963, Glaciological Studies on Ice Island T-3, J. Glaciology 4, pp. 709-730.

Ragle R.H., Blair R.G. & Persson L.E., 1964, Ice Core Studies of Ward Hunt Ice Shelf, 1960, J. Glaciology, Vol. 5, No 37, pp. 39-59.

Smith D.D., 1960, Origin of Parallel Pattern of Meltwater Lakes on Fletcher's Ice Island T-3, Report of the International Geological Congress, XXI Session, Norden.

Smith D.D., 1964, Ice Lithologies and Structure of Ice Island Arlis II, J. Glaciology, Vol. 5, No 37, pp. 17-38.

Stogryn A.& Desargant G.J., 1985, The Dielectric Properties of Brine in Sea Ice at Microwave Frequencies, IEEE Trans. Antennas Propagat., Vol. AP-33, No 5, pp. 523-532.

Tsang L., Kubacsi M.C. & Kong J.A., 1981, Radiative Transfer Theory for Active Remote Sensing of a Layer of Small Ellipsoidal Scatterers, Radio Science, Vol. 16, No 3, pp. 321-329.

Tsang L. & Kong J.A., 1992, Scattering of Electromagnetic Waves from a Dense Medium Consisting of Correlated Mie Scatterers With Size Distribution and Application to Dry Snow, J. Electromagn. Waves and Applications, Vol. 6, No 3, pp. 265-286.

Ulaby F.T., Moore R.K. & Fung A.D., 1982, Microwave Remote Sensing, Vol. II: Radar Remote Sensing and Surface Scattering and Emission Theory (Massachusetts: Addison-Wesley Publ. Comp.).

Ulaby F.T., Moore R.K. & Fung A.D., 1986, Microwave Remote Sensing, Vol. III: From Theory to Applications (Washington: Artech House Inc.).

Wen B., Tsang L., Winebrenner D.P. & Ishimaru A., 1990, Dense Medium Radiative Transfer Theory: Comparison With Experiment and Application to Microwave Remote Sensing and Polarimetry, IEEE Trans. Geosc. Remote Sensing, Vol. 28, No 1, pp. 46-59.